

Article

Effect of Sodium Phosphate and Cellulose Ethers on MgO/SiO₂ Cements for the 3D Printing of Forsterite Bioceramics

Lorenzo Cheli, Massimo Bonini and Monica Tonelli * 

Department of Chemistry “Ugo Schiff” and CSGI, University of Florence, Via Della Lastruccia 3, Sesto Fiorentino, 50019 Florence, Italy; lorenzo.cheli@edu.unifi.it (L.C.); massimo.bonini@unifi.it (M.B.)

* Correspondence: monica.tonelli@unifi.it

Abstract: Magnesium silicate ceramics are promising materials for bone tissue regeneration and can be prepared through 3D printing of magnesium oxide/silica (MgO/SiO₂) cement pastes followed by calcination. Despite the growing interest in these formulations, additive manufacturing technology has only recently been explored for these cements, and the effects of admixtures and additives on such printing inks remain largely unexplored. In this study, we prepared various MgO/SiO₂ cement formulations with differing amounts of sodium orthophosphate, a setting retarder, and cellulose ethers, used as rheo-modifiers. The samples’ setting properties were investigated, and printing parameters were properly adjusted. The most promising formulations were then 3D printed and calcined to obtain forsterite bioceramics, which were further characterized using confocal Raman microscopy, scanning electron microscopy, atomic force microscopy, gas porosimetry, and compressive strength tests. Our results revealed that the cellulose derivatives influence the printability of the MgO/SiO₂ formulations without affecting the hardening time, which can be adjusted by the addition of sodium phosphate. The use of fine-tuned formulations allowed for the preparation of 3D-printed forsterite bioceramics, potentially suitable for biological applications as cancellous bone scaffolds.

Keywords: 3D printable cements; magnesium silicate hydrate; biocompatible magnesium silicates; bioactive ceramics; forsterite; bone scaffolds



Citation: Cheli, L.; Bonini, M.; Tonelli, M. Effect of Sodium Phosphate and Cellulose Ethers on MgO/SiO₂ Cements for the 3D Printing of Forsterite Bioceramics. *Appl. Sci.* **2024**, *14*, 4410. <https://doi.org/10.3390/app14114410>

Academic Editors: Agata Lisińska-Czekaj and Tomasz Pikula

Received: 22 April 2024

Revised: 15 May 2024

Accepted: 19 May 2024

Published: 23 May 2024



Copyright: © 2024 by the authors. Licensee MDPI, Basel, Switzerland. This article is an open access article distributed under the terms and conditions of the Creative Commons Attribution (CC BY) license (<https://creativecommons.org/licenses/by/4.0/>).

1. Introduction

Magnesium silicate hydrate (M-S-H) cements have recently been explored as 3D printable inks for creating crystalline bioceramics suitable for use as cancellous bone scaffolds [1]. The increasing demand for bone substitutes has driven the development of materials that possess biological and physical properties akin to human bone [2]. In this context, various materials, including hydroxyapatite [3], calcium and magnesium phosphate materials [4,5], silicates [6], and bioactive glasses [7] have been developed. Despite the widespread use of calcium phosphate and hydroxyapatite, their slow resorption rates [8,9] have prompted interest in silicate bioceramics like clinoenstatite (MgSiO₃) and forsterite (Mg₂SiO₄) due to their favorable degradation rates, mechanical properties, biocompatibility, and osteostimulation [10]. In particular, magnesium silicate ceramics, namely clinoenstatite (MgSiO₃) and forsterite (Mg₂SiO₄), were recently demonstrated as one of the most promising materials for bone tissue regeneration, thanks to their good resorption rate, mechanical properties, biocompatibility, and osteostimulation [11–16].

Bioactive ions such as Mg and Si within these bioceramics have been reported to enhance the adhesion, proliferation, differentiation, and mineralization of mesenchymal stem cells, facilitating the osseointegration of the porous scaffolds [12], which in turn would favor the osseointegration of the porous scaffold. Typically, MgSiO₃ and Mg₂SiO₄ are synthesized via a precipitation method to produce an amorphous gel phase (M-S-H, (MgO)_x-(SiO₂)_y-(H₂O)_z) that requires high-temperature treatment to achieve the desired crystalline bioceramic phases [14,16–19]. M-S-H also serves as the main binder in a recently

developed eco-sustainable cement [20–24], and some of the authors recently demonstrated that clinoenstatite and forsterite can be prepared starting from MgO/SiO₂ pastes [1].

This research builds on the capability of such cements to be 3D printed [1,25,26], offering significant advantages [27] in both building and biomedical applications by enabling the direct creation of personalized bioceramics upon calcination. However, despite the potential and growing interest in using M-S-H for diverse applications, the preparation of complex structures via 3D printing has only recently been explored, with many cementitious materials previously printed over the past two decades, including calcium and magnesium phosphate cements [28–31], sulphoaluminate cement [32], and calcium silicate hydrate cements [33–39]. Recent studies have highlighted the need for additives like superplasticizers and suspension aids to achieve extrudable M-S-H formulations [1,25,26]. These additives are crucial for maintaining the fluidity and plasticity required for printing, yet their effects on the properties of the resulting inks have not been fully explored. To extrude magnesium-based cements, Panda et al. reported the use of a superplasticizer (sodium hexamethaphosphate) [25], while Khalil et al. incorporated in the paste various additives: a plasticizer (polycarboxylate ether), a suspension-aid additive (hydroxyethyl-cellulose), a hydration agent (magnesium acetate), and a defoamer (a non-ionic surfactant) [26]. Nevertheless, even though these additives are essential for the production of extrudable 3D printable ink, their effect has been left unexplored so far. Moreover, achieving the delicate balance between fluidity for easy extrusion and sufficient stiffness to prevent deformation is a critical challenge in 3D printing cements.

It is worth noting that the 3D printing of setting cements faces two conflicting requirements: the paste must be fluid enough to ensure homogeneous mixing and easy extrusion throughout the printing process, while the extruded paste must be stiff enough to prevent shape variations and bleeding. Cellulose derivatives are commonly used in various 3D printable inks [40–42], including calcium silicate hydrate formulations [43], to meet these requirements due to their well-established water-carrying capacity. According to the literature, cellulose derivatives influence the viscosity of cementitious materials through adsorption on the cement surface [43–47]. These derivatives are not only suitable for bioceramics due to their biocompatibility, biodegradability, and hydrophilicity, but they also play a crucial role in managing the physical properties of the paste [44,48]. Furthermore, biocompatible plasticizers can be used to achieve the desired fluidity of pastes, thus facilitating easier 3D printing [49–51]. These plasticizers also delay the hardening process, which is essential to avoid premature setting. To this purpose, sodium orthophosphate (OP) and hexametaphosphate have been shown to enhance the formation of MgO/SiO₂ cement phases, while effectively retarding their setting mechanisms [52].

Understanding the combined effects of these plasticizers and suspension-aid additives is paramount for properly formulating 3D printable M-S-H cements, which are essential for creating biologically relevant ceramic materials with tailored shapes. This work explores the impact of OP as a setting retarder in conjunction with cellulose ethers, such as hydroxypropyl methylcellulose (HPMC) and carboxymethyl methylcellulose (CMC), which serve as viscosity-modifying agents in MgO/SiO₂ formulations. To optimize these formulations, a comprehensive approach was adopted, encompassing the monitoring of hardening times via the Gillmore test, the evaluation of printability, and structural analysis through X-ray diffraction (XRD). Following these preparatory steps, the most promising pastes were 3D printed and calcined at 1000 °C to create bioceramic scaffolds. These scaffolds were then extensively characterized using Raman confocal microscopy, scanning electron microscopy (SEM), atomic force microscopy (AFM), gas porosimetry, and compressive strength tests to assess their potential applications as bone scaffolds.

2. Materials and Methods

2.1. Materials

Periclase (MgO ≥ 99% trace metal basis, 325 mesh) was supplied by Sigma-Aldrich (Burlington, MA, USA). Elkem Microsilica Grade 940 U was kindly provided by Elkem,

Oslo, Norway (dry silica fume, $\text{SiO}_2 > 90\%$, BET specific surface area = $4.33 \text{ m}^2/\text{g}$). Hydroxypropyl methylcellulose (HPMC, viscosity of 2% HPMC in H_2O $\sim 21.8 \text{ mPa}\cdot\text{s}$, Product No. 09963, batch BCCC1820) and carboxymethyl methylcellulose (CMC, viscosity of 4% CMC in H_2O $\sim 106 \text{ mPa}\cdot\text{s}$, Product No. C5678, batch 107K0109) were purchased from Sigma-Aldrich. Sodium orthophosphate (OP) was purchased from Aldrich. Milli-Q water was used throughout all the experiments. All materials were used as received.

2.2. Preparation of the Cement Formulations

Cements were prepared by dry mixing MgO and SiO_2 powders in a 2/1 molar ratio together with different amounts of OP (P/Mg ratios of 0, 0.01, 0.02, and 0.03). Then, the cement pastes were prepared by adding HPMC or CMC water solutions at different concentrations to achieve a water-to-solid weight ratio (w/s) of 1.25 and to obtain different concentrations of cellulose (5, 7.5, 10, and 12.5 wt% of HPMC or CMC). An abbreviated notation is used throughout this paper to refer to samples prepared using different amounts of cellulose and P/Mg ratios. For example, HPMC5_P0 refers to the formulation containing 5 wt% of HPMC and a P/Mg ratio of 0, while CMC10_P2 refers to 10 wt% of CMC and a P/Mg ratio of 0.02.

2.3. Characterization of MgO/SiO_2 Cements

2.3.1. Fluidity and Hardening

The effect of OP and HPMC/CMC on the consistency and fluidity of the cement pastes was initially evaluated by analyzing the aspects of the fresh pastes. In a typical experiment, after mixing for about 30 s, freshly prepared pastes were poured on millimeter grid paper and allowed to harden at room temperature. Cement pastes were checked every 15 min with a spatula to manually control their setting and to understand if the additives influenced the time of hardening of the cements.

2.3.2. Gillmore Test

The initial and final setting times of cement pastes were measured by means of a Gillmore apparatus (Matest, Bergamo, Italy), according to ASTM standard C-266 [53] for the characterization of the setting of cements. Freshly prepared pastes were poured in plastic molds (diameter 1 cm) and allowed to harden at room temperature, while the surface was tested every 2 min with the Gillmore apparatus. Cement is considered to attain its initial and final setting times when its surface bears the initial and final Gillmore needle, respectively, without appreciable indentation (“initial setting” needle diameter 2.12 mm, weight 113.4 g and “final setting” needle diameter 1.06 mm, weight 453.6 g).

2.3.3. Printability of the Cement Pastes

The cement pastes with longer setting times were selected for the 3D printing tests. These formulations were 3D printed using a tapered G16 needle, with an Engine Standard Resolution 3D printer developed by HyRel (Norcross, GA, USA) equipped with a modular head KRA-15. In this study, one 2D structure and one 3D macroporous structure were drawn using the Free-CAD program, sliced through PrusaSlic3r software 2.5.2 and printed (Repetrel software 4.2.597). The 2D shape was printed with a layer thickness of 1.2 mm at different rates (2.5, 5, 7.5, and 10 mm/s) to assess the printability of the inks. Images of the printouts were taken with an optical microscope, converted to duotone (black and white) images, and the maximum profile peak height parameter (R_p) was used to evaluate the printability of the inks. To this purpose, the shape fidelity [54] was assessed using R_p through the evaluation of the maximum diameter observed for the printed filament with respect to its design. The roughness parameters were calculated from the images using the ImageJ program, and lower R_p values were related to better printability, which was connected to better shape fidelity. The 3D shape ($1 \times 1 \times 1 \text{ cm}^3$) was printed at 5 mm/s with a layer thickness of 1.2 mm at an infill ratio of 80%.

2.3.4. X-ray Diffraction

Selected cement formulations were stored for 2 days at 37 °C (1 day at RH \approx 98% and 1 day underwater [55]), freeze-dried to arrest the hydration reaction, and characterized by means of XRD. Data were collected with a D8 Advance with DAVINCI design (Bruker, Milan, Italy), using Cu Ka radiation as an X-ray source (wavelength λ = 1.542 Å), at 40 kV and 40 mA, in a 2 θ range of 5–70°, with a step size of 0.03° and a time per step of 0.3 s. Before the analysis, set cements were ground with a mortar and pestle and flattened on a Si zero-background sample holder. Peaks' assignment was based on the Powder Diffraction Files (PDF) of the database of the International Centre for Diffraction Data.

2.4. Preparation of the Bioceramics

Selected 3D-printed cements (stored for 1 day at 37 °C with an RH of \approx 98% and for 1 day underwater at 37 °C [55]) were calcined at 1000 °C for 2 h to convert them into bioceramics [1].

2.5. Characterization of the Bioceramics

2.5.1. Confocal Raman Microscopy

Raman analysis and 2D mapping were performed on 3D printed bioceramics with a Renishaw inVia Qontor confocal MicroRaman system (Wotton-under-Edge, UK) equipped with a 532 nm laser (Nd:YAG solid state type, 50 mW, 1800 l/mm grating), a front illuminated CCD camera, and a research-grade Leica DM 2700 microscope (Wetzlar, Germany) equipped with a 20 \times objective (theoretical spot size 2.4 μ m). Raman spectra were acquired in the spectral range 170–1910 cm^{−1}, and maps were collected with a step size of 2.5 μ m.

2.5.2. Field Emission-Scanning Electron Microscopy (FE-SEM)

FE-SEM images were collected on bioceramic cross-sections with a field-emission SIGMA microscope (Carl Zeiss Microscopy, Munich, Germany). Specimens were fixed to aluminum stubs by means of conductive tape. The accelerating potential was 2.00 kV, while the working distance was \sim 8 mm. Images were acquired using a standard secondary electron detector.

2.5.3. Atomic Force Microscopy (AFM)

AFM was performed on 3D-printed bioceramics' surfaces with a Park System XE-7 microscope (Suwon, Korea) equipped with PPP-NCHR 10M probes (tip radius of curvature < 10 nm) in non-contact mode. Image processing (flattening) and calculation of the roughness parameters were performed using the Park Systems XEI software 1.8.2.

2.5.4. Gas Porosimetry

The Specific Surface Area (SSA) and Pore Size Distribution (PSD) of the 3D-printed bioceramics were measured by means of a 3Flex analyzer (Micromeritics, Norcross, GA, USA), using nitrogen as an adsorptive gas. The samples were broken into small pieces and inserted in the sample holders. Prior to the measurements, samples were outgassed for 1 h at 120 °C. SSA was obtained using the Brunauer Emmett–Teller (BET) method [56], while the pore size distribution was estimated using Barrett–Joyner–Halenda (BJH) analysis [57].

2.5.5. Compressive Strength Test

The compressive strength of 3D printed bioceramic scaffolds was tested by performing compression experiments with a custom-built apparatus. Cubic 3D printed specimens were subjected to a gradually increasing load applied to the top surface until a rupture occurred. Five samples were prepared for each selected composition, and the reported results are the average compressive strength \pm the associated standard deviation.

3. Results and Discussion

3.1. Characterization of the Cement Pastes

3.1.1. Preliminary Experiments: Selection of the Formulations

As introduced earlier, phosphate additives can be incorporated into MgO/SiO_2 formulations to improve the fluidity of the cement paste without increasing the amount of water used. Sodium orthophosphate (OP) has been recently demonstrated to be the most efficient fluidificant for M-S-H cements [52]. Here, the potential effects of combining Hydroxypropyl methylcellulose/Carboxymethyl methylcellulose (HPMC/CMC) with OP on the consistency and fluidity of the cements were initially evaluated by manually monitoring the hardening of the pastes. As described in Section 2.3.1, the formulations were periodically checked with a spatula to control their setting times and to understand how the combined use of these additives influenced the hardening of the pastes. The results of the tests, reported in Figure 1, reveal that the presence of cellulose derivatives does not influence the hydration reaction, and thus the hardening of the cements, while OP increases the setting time and the fluidity of the pastes up to a threshold value. In fact, systems with a P/Mg ratio of 0.02 showed the longest setting times and highest fluidity, regardless of the HPMC/CMC concentration. The presence of a threshold value for phosphate as a water-reducing and retarding admixture was already observed in analogous systems, where 1 wt% of $(\text{NaPO}_3)_6$ was reported as the correct dosage of fluidificant (corresponding to a P/Mg ratio of about 0.01) to achieve the highest fluidity for $\text{Mg}(\text{OH})_2/\text{silica fume}$ pastes [58]. As a comparison, other M-S-H extrudable inks were previously prepared using 1.5–2.5% of sodium hexametaphosphate [25] or without phosphates [1]. Here, a P/Mg ratio of 0.02 was selected to extend the setting times of the investigated pastes as much as possible and facilitate the 3D printing of such formulations. Considering that HPMC and CMC did not affect the appearance and hardening of our samples, only two cellulose concentrations were selected to evaluate their effect on the physico-chemical properties of the 3D printed materials: 5 wt% and 10 wt% of HPMC/CMC. According to the literature, these water retention additives could influence the strength of 3D-printed calcium silicate cements [47], and here their effect on magnesium silicate cements was preliminary investigated.

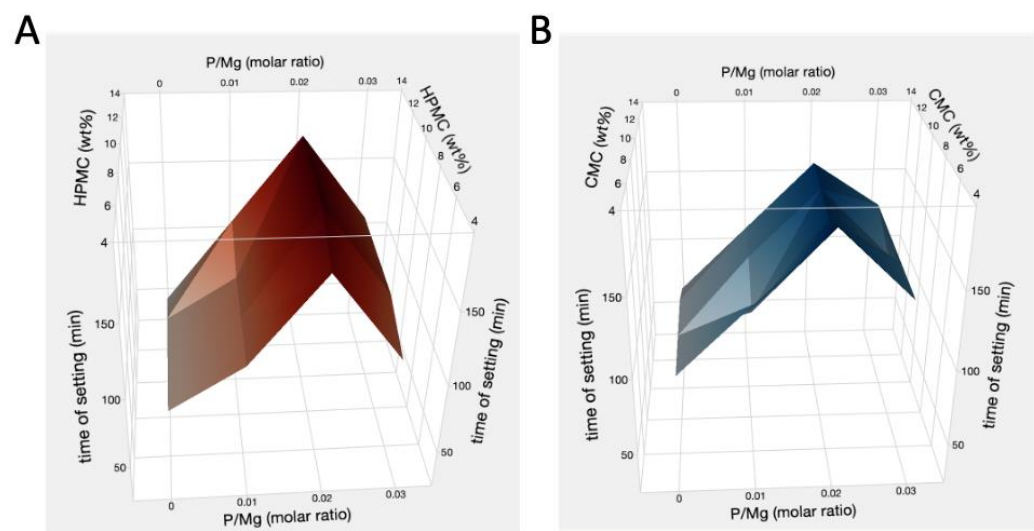


Figure 1. Times of setting of the pastes plotted in function of the concentration of OP and HPMC (A) or CMC (B) amounts. The setting of the pastes was evaluated every 15 min with a spatula, until the pastes hardened to a non-injectable cement (identified as the time of setting).

3.1.2. Printability and Setting Properties

Considering the complex equilibria that regulate the extrusion process of cement-based materials, achieving and assessing printability is particularly challenging. Three

main requirements must be met: (i) the paste should have the appropriate setting time, allowing for extrusion before hardening since concrete mixtures can be injected from a nozzle and are only printable until they begin to set; (ii) the formulation should be stiff enough to maintain the required shape and prevent collapse; (iii) the formulation should be fluid enough to avoid the formation of voids and incomplete structures. Here, the consistency and fluidity of the cement pastes were initially evaluated by analyzing the aspect of the pastes poured on millimeter grid paper immediately after mixing, using a simplified version of the slump test commonly used to measure the workability of concrete [59]. The appearance of two discarded formulations (too dry on the left, too fluid on the right) is shown in Figure 2A, along with the appearance of the selected pastes (Figure 2B) and the results of the Gillmore test (Figure 2C). According to the results, all of the selected pastes appear fluid enough to be easily workable and extrudable but stiff enough to maintain their shape and prevent deformations (Figure 2B). Parallely, the setting times, crucial parameters for the 3D printing of toughening materials, were quantitatively evaluated on the pre-selected formulations using the Gillmore test before proceeding with the printability tests. These experiments allowed for correlating the observations reported in Section 3.1.1 with the measured hardening times, t_1 and t_2 . According to the results, all pastes displayed similar initial and final setting times ($t_1 \approx 50$ min and $t_2 \approx 240$ min), indicating very long setting periods compatible with the preparation of complex 3D printed shapes that require extended printing durations.

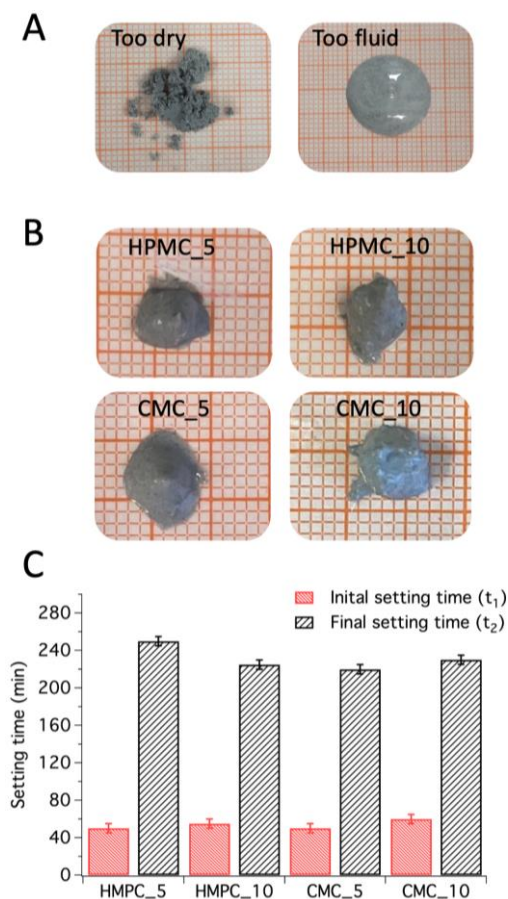


Figure 2. Pictures of some discarded formulations inappropriate for 3D printing (A), and of the selected pastes (B) 30 s after mixing; initial and final setting times obtained through the Gillmore test (C).

Having established that the fluidity of the pastes was suitable for 3D printing, we evaluated their ability to achieve desired outcomes, specifically to avoid structural collapse from excessive workability and the presence of voids from insufficient workability [60]. For

this purpose, we used printability parameters [54,61,62] to qualitatively and quantitatively describe the geometrical differences between the designed print and the experimental pattern. The samples were printed by extruding the pastes until clogging occurred. Initially, the 2D shapes, prepared at different printing rates, were visually evaluated to assess the presence of voids or incomplete prints. Table 1 reports the roughness parameters calculated from the images, along with a qualitative characterization of their extrudability. In some cases, we achieved a complete 2D structure where the flow rate could be well controlled and regulated by the extrusion force, confirming that the ink was suitable for continuous and controllable extrusion [62]. In other cases, the pastes exhibited non-continuous extrusion, attributable to inadequate flow behavior. The roughness parameter R_p , calculated using ImageJ from the images, was used to evaluate the printing quality of the selected formulations by comparing the designed pattern with the experimental prints (see Figure 3A). The optimal printing speed for extruding the investigated MgO/SiO₂ pastes was found to be 5 mm/s, which achieved the best results with the lowest R_p values (also see Table 1), associated with better shape fidelity. A lower printing velocity of 2.5 mm/s could also be used to achieve extrudable pastes, but this would lead to poorer printability (higher R_p values) and would be more time-consuming. Higher printing velocities were unsuitable for these samples as they led to the formation of voids and incomplete shapes, thus being inappropriate for the preparation of 3D structures. For example, Figure 3B shows images of two tridimensional prints: one obtained under the optimal selected printing conditions (Figure 3B, top), allowing for the preparation of customized ceramics, and another using non-optimized printing parameters (Figure 3B, bottom), inappropriate for the preparation of forsterite scaffolds.

Table 1. R_p roughness parameter of the 2D printed cements extruded at different velocities, together with an evaluation of their extrudability.

Sample	Printing Speed [mm/s]	R_p [mm]	Extrudability
HPMC_5	2.5	0.44	Continuous and controllable
	5	0.35	Continuous and controllable
	7.5	0.43	Continuous and controllable
	10	0.49	Discontinuous
HPMC_10	2.5	0.37	Continuous and controllable
	5	0.36	Discontinuous
	7.5	0.47	Discontinuous
	10	0.36	Discontinuous
CMC_5	2.5	0.19	Discontinuous
	5	0.18	Continuous and controllable
	7.5	0.47	Discontinuous
	10	0.23	Discontinuous
CMC_10	2.5	0.18	Continuous and controllable
	5	0.15	Continuous and controllable
	7.5	0.50	Discontinuous
	10	0.29	Discontinuous

When comparing different formulations, it is clear that cellulose derivatives, which influence the plasticity of the formulations, can affect the printability quality of the samples. Specifically, samples containing HPMC exhibited a higher roughness R_p than those using CMC (see Table 1), indicating that CMC should be preferred when designing 3D printable M-S-H.

To understand if the use of different cellulose derivatives would also influence the phases forming during the hardening of the cements, printed samples were investigated using XRD after 2 days of hydration, as reported in Figure 4. All cement-based samples display a similar bulk composition, confirming the formation of an abundant amorphous

binder phase, M-S-H, upon the hydration of MgO/SiO₂. The presence of some unreacted Mg(OH)₂ is reasonably ascribed to the use of abundant MgO, since all samples were prepared using MgO/SiO₂ in a 2/1 molar ratio to favor the formation of the Mg₂SiO₄ ceramic phase upon heating.

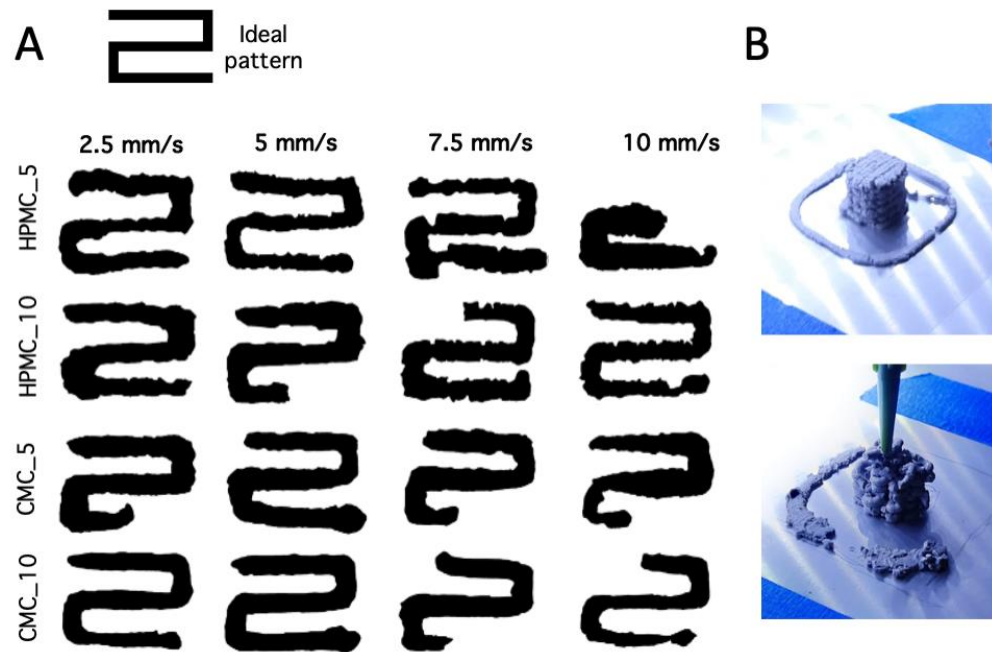


Figure 3. (A) Top view black/white images of 2D printed cements prepared at different printing velocities; (B) pictures of a good (top) and bad (bottom) 3D printed cement.

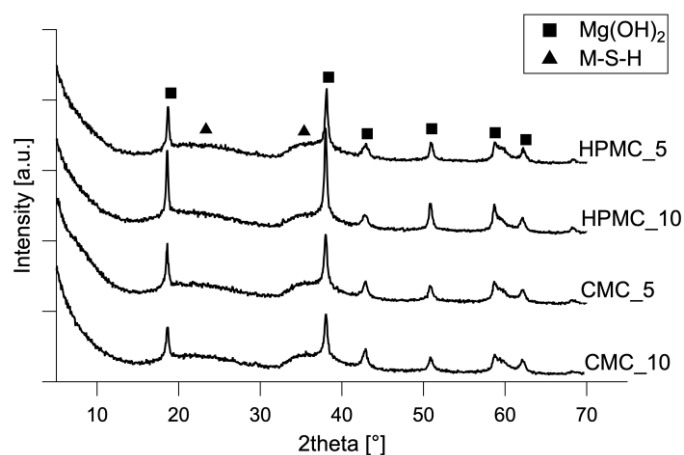


Figure 4. XRD patterns of cements after 2 days of hydration.

Thus, set 3D-printed cements were employed to prepare the bioceramics of interest, as described in Section 2.4.

3.2. Characterization of the 3D-Printed Bioceramics

Figure 5 shows the 2D confocal Raman maps acquired on the cross-sections of the printed bioceramics. According to the results, Mg₂SiO₄ is the main component of all samples, but when using 5% of HPMC or 5% of CMC, some MgSiO₃ is also present, mostly accumulated on the surface (colored in green in Figure 5). Thus, the use of different cellulose derivatives (HPMC or CMC), fundamental for achieving satisfactory printing parameters, did not influence the composition of the forming bioceramics. At the same time, it is important to note here that 3D scaffolds made of pure forsterite could be prepared only

when using 10% of HPMC/CMC, suggesting that the amount of cellulose influences the forming phases. This result can be attributed to the water regulatory effect of these cellulose derivatives, which are expected to affect the water availability in the cement formulations, thus influencing the hydration reaction of MgO/SiO_2 , which in turn impacts the bioceramics forming upon thermal treatment of M-S-H. In fact, at the sub-nanometric level, M-S-H can resemble a mixture of chrysotile ($\text{Mg}_3\text{Si}_2\text{O}_5(\text{OH})_4$) and talc ($\text{Mg}_3\text{Si}_4\text{O}_{10}(\text{OH})_2$) [22], and the water-carrying capacity of HPMC/CMC could influence these hydration products forming when MgO/SiO_2 reacts with water to form M-S-H.

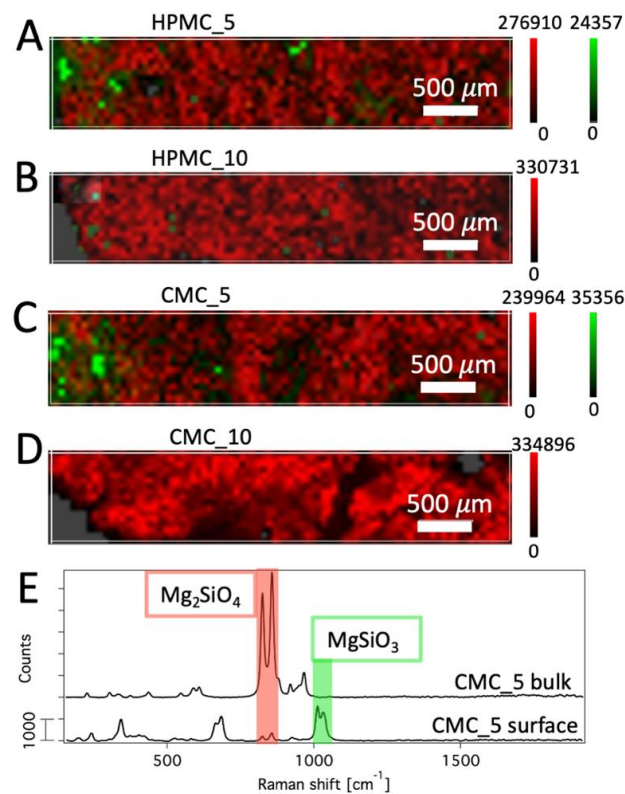


Figure 5. Confocal Raman maps collected on the cross-sections of printed samples HPMC_5 (A), HPMC_10 (B), CMC_5 (C), and CMC_10 (D); and Raman spectra of CMC_5 bulk (top) and surface (bottom) (E), where the red and green regions highlight the peaks of forsterite and clinoenstatite selected for the mapping, respectively. All mapped samples (A–D) expose the external surfaces on the left.

Figure 6 shows the SEM images collected on the cross-sections of the printed bioceramics. In all cases, the morphology of the samples is homogeneous, and at small magnification (Figure 6, images on the left), we can see the macro-porous nature of the samples' morphology. At higher magnification (Figure 6, images on the right), we can observe polydisperse agglomerated objects, ascribable to forsterite and, eventually, clinoenstatite phases [14,16,63].

The topography of the printed bioceramics was also studied through AFM (Figure 7), to gain information on the roughness of the investigated samples, taking into account that micro/nano-topographies resembling the structure of natural bone could improve the biological performances. The results confirm the presence of rounded, agglomerated phases, as observed by means of SEM, with sizes ranging from tens of nm to a few μm. Table 2 reports the average values of roughness (R_a , arithmetic mean roughness) calculated on different maps. According to the results, the samples display varying roughness levels, indicating that the cellulose derivatives can affect this important parameter. In particular, when using 10% of HPMC or CMC, the surfaces display smaller particles (see Figure 7) and lower R_a values (Table 1), which could be appropriate for the successful deposition of

hydroxyapatite and thus for the preparation of scaffolds with good biocompatibility, since scaffolds containing forsterite and displaying similar values of roughness were recently reported for the successful deposition of hydroxyapatite [64,65].

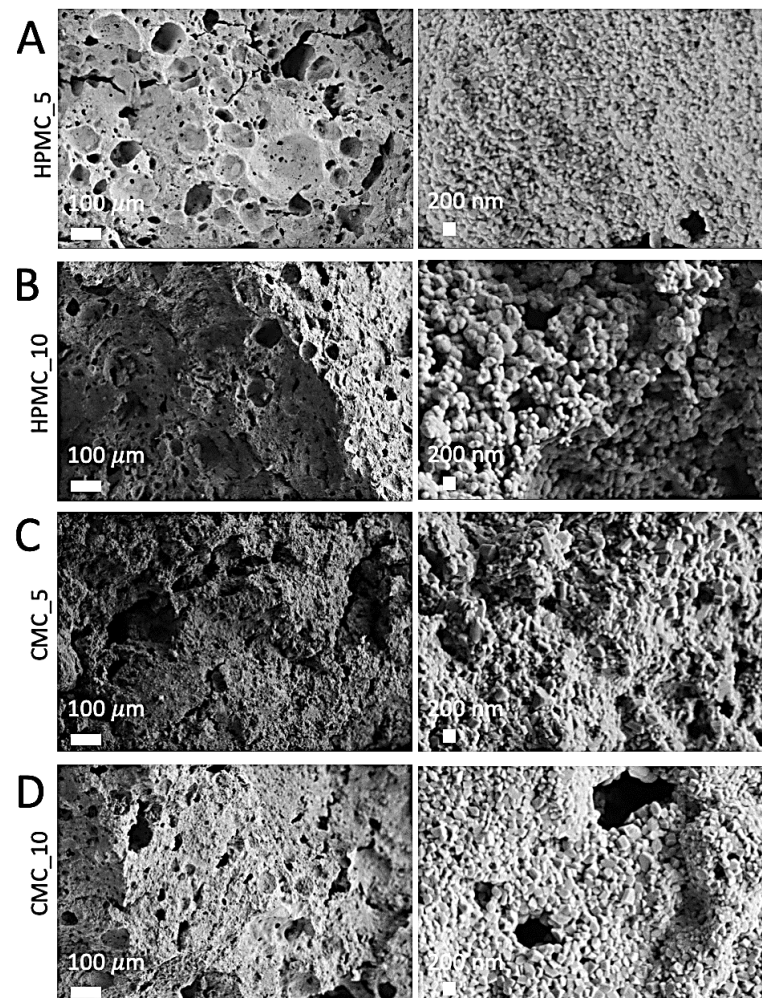


Figure 6. FE-SEM images of the cross-sections of the printed bioceramics HPMC_5 (A), HPMC_10 (B), CMC_5 (C), and CMC_10 (D).

Table 2. Roughness Ra, SSA, total pore volume, and results of the compressive strength tests performed on the 3D-printed bioceramics. The reported arithmetic mean roughness values (Ra) are the average of five maps acquired on different regions of the samples \pm standard deviation. The compressive strength values are the average of three tests \pm standard deviation.

Sample	Ra (nm)	SSA (m ² /g)	Total Pore Volume (mL/g)	Compressive Strength (MPa)
HPMC_5	464 \pm 152	5.6	0.035	0.55 \pm 0.16
HPMC_10	212 \pm 67	3.7	0.017	0.51 \pm 0.11
CMC_5	360 \pm 72	3.5	0.016	0.40 \pm 0.06
CMC_10	180 \pm 94	2.1	0.013	0.38 \pm 0.05

The porosity of the microstructure and the structural features were further investigated by means of gas porosimetry and compressive strength tests (see Table 2). We observed that higher amounts of HPMC/CMC lead to scaffolds with lower specific surface areas and total pore volumes, which could be ascribed to an enhanced hydration reaction. Indeed, the porosity assessed by BET/PSD experiments (3–200 nm) can be used to gain information on

the structure's phases, as it is closely related to the complex network of pores characteristic of dried cementitious materials [24]. As anticipated, cellulose derivatives are considered responsible for the regulation of water in the cementitious pastes, which plays a major role in the formation of the hydrated reaction products. According to results gained from confocal Raman experiments, when using 10% of HPMC or CMC, only Mg_2SiO_4 forms. Considering that all samples were prepared with an Mg/Si molar ratio of 2/1, we can assume that in the presence of abundant cellulose derivatives, we achieved very efficient reaction conditions, consuming almost all the reactants and thus resulting in smaller SSA and total pore volumes. At the same time, the samples prepared with 5 wt% of HPMC/CMC show compressive strengths very similar to their counterparts containing 10 wt% of cellulose. This could be explained considering that the mechanical properties are related to the total porosity (from nanoscale pores up to millimetric pores), and the strength is highly affected by large pores [66]. Nonetheless, all these values could be compatible with biological applications as cancellous bone scaffolds [67].

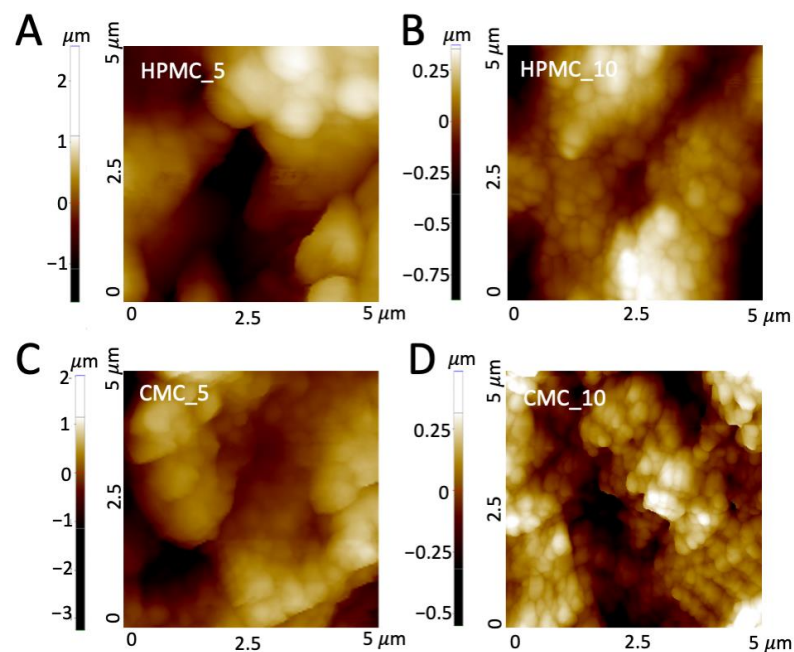


Figure 7. AFM maps of the printed bioceramics HPMC_5 (A), HPMC_10 (B), CMC_5 (C), and CMC_10 (D).

4. Conclusions

The goal of this study was to explore the effects of orthophosphate (OP) and cellulose derivatives on MgO/SiO_2 formulations for producing 3D-printed bioceramics. These formulations recently raised growing interest in additive manufacturing technology and were demonstrated as efficient starting materials for the preparation of clinoenstatite and forsterite bioceramics. However, the preparation of complex structures through 3D printing has only recently been explored for such cements, and even though some additives were already reported as essential for the obtainment of an extrudable ink, their effect on such formulations has been left unexplored so far. Here, we meticulously characterized magnesium silicate hydrate (M-S-H) cements containing various admixtures, which served as the basis for developing 3D printing inks. Upon calcination, these inks yielded Mg_2SiO_4 -biologically relevant ceramics. Our findings indicate that sodium orthophosphate can be utilized in M-S-H pastes as a water-reducing admixture with retardant properties, extending the setting times and maintaining sufficient fluidity for easy extrusion during printing. Furthermore, when used in conjunction with OP, HPMC and CMC did not alter the hardening times of the MgO/SiO_2 cement pastes but acted as beneficial suspension aids. The presence of cellulose derivatives, already used as viscosity modifiers in other cementitious systems,

notably influenced the water dynamics within the cement formulations, thereby impacting their printability.

The printing parameters for these cement pastes were carefully adjusted, and selected formulations were successfully 3D printed and converted into forsterite bioceramics. Confocal Raman mapping highlighted the influence of cellulose on the formation of different ceramic phases. Both AFM and SEM analyses confirmed the achievement of homogeneously rough surfaces with excellent interlayer adhesion. Additionally, gas porosimetry and compressive strength tests underscored the porous nature of the materials and suggested that these samples could be appropriate for biological applications, particularly as scaffolds for cancellous bone.

This study not only enhances our understanding of the interplay between additives and cement pastes in 3D printing but also sets the stage for future work aimed at refining these bioceramic formulations. By further optimizing the interactions of components and printing parameters, we can advance towards tailored biomedical applications, potentially leading to breakthroughs in personalized medicine and implantable scaffold technologies.

Author Contributions: Conceptualization, M.B. and M.T.; investigation, L.C. and M.T.; formal analysis, L.C., M.B. and M.T.; writing—original draft preparation, L.C. and M.T.; writing—review and editing, M.B. and M.T.; funding acquisition, M.B. and M.T. All authors have read and agreed to the published version of the manuscript.

Funding: This research was funded by CSGI (Consorzio Interuniversitario per lo Sviluppo dei Sistemi a Grande Interfase) and MIUR-Italy (“Progetto Dipartimenti di Eccellenza 2018–2022” and “Dipartimenti di Eccellenza 2023–2027 DICUS 2.0” allocated to Department of Chemistry “Ugo Schiff”, University of Florence). The research was also funded under the National Recovery and Resilience Plan (NRRP), Mission 4 Component 2 “Dalla ricerca all’impresa”—Call for tender No. 341 of 15/03/2022 of Italian Ministry of Research funded by the European Union—NextGenerationEU, Project title “3A-ITALY - Made-in-Italy circolare e sostenibile”, CUP: B83C22004890007.

Institutional Review Board Statement: Not applicable.

Informed Consent Statement: Not applicable.

Data Availability Statement: The data presented in this study are available in the article.

Conflicts of Interest: The authors declare no conflicts of interest. The funders had no role in the design of the study; in the collection, analyses, or interpretation of data; in the writing of the manuscript; or in the decision to publish the results.

References

1. Tonelli, M.; Faralli, A.; Ridi, F.; Bonini, M. 3D Printable Magnesium-Based Cements towards the Preparation of Bioceramics. *J. Colloid Interface Sci.* **2021**, *598*, 24–35. [\[CrossRef\]](#)
2. Nabiyouni, M.; Brückner, T.; Zhou, H.; Gbureck, U.; Bhaduri, S.B. Magnesium-Based Bioceramics in Orthopedic Applications. *Acta Biomater.* **2018**, *66*, 23–43. [\[CrossRef\]](#) [\[PubMed\]](#)
3. Pei, X.; Ma, L.; Zhang, B.; Sun, J.; Sun, Y.; Fan, Y.; Gou, Z.; Zhou, C.; Zhang, X. Creating Hierarchical Porosity Hydroxyapatite Scaffolds with Osteoinduction by Three-Dimensional Printing and Microwave Sintering. *Biofabrication* **2017**, *9*, 45008. [\[CrossRef\]](#) [\[PubMed\]](#)
4. Zhang, B.; Sun, H.; Wu, L.; Ma, L.; Xing, F.; Kong, Q.; Fan, Y.; Zhou, C.; Zhang, X. 3D Printing of Calcium Phosphate Bioceramic with Tailored Biodegradation Rate for Skull Bone Tissue Reconstruction. *Bio-Des. Manuf.* **2019**, *2*, 161–171. [\[CrossRef\]](#)
5. Leng, B.; Jin, X.; Lin, Q.; Chen, L.; Wang, Y.; Du, Z.; Lin, K.; Chang, J.; Gu, X.; Wang, C. A Comparative Study of Proliferation and Osteogenic Differentiation of Rat Adipose-Derived Stem Cells in β -Tricalcium Phosphate (β -TCP), Forsterite (Mg_2SiO_4) and Clinoenstatite (MgSiO_3). *Chin. Sci. Bull.* **2013**, *58*, 3033–3042. [\[CrossRef\]](#)
6. Feng, X.; Wu, Y.; Bao, F.; Chen, X.; Gong, J. Comparison of 3D-Printed Mesoporous Calcium Silicate/Polycaprolactone and Mesoporous Bioactive Glass/Polycaprolactone Scaffolds for Bone Regeneration. *Microporous Mesoporous Mater.* **2019**, *278*, 348–353. [\[CrossRef\]](#)
7. Yang, C.; Wang, X.; Ma, B.; Zhu, H.; Huan, Z.; Ma, N.; Wu, C.; Chang, J. 3D-Printed Bioactive Ca_3SiO_5 Bone Cement Scaffolds with Nano Surface Structure for Bone Regeneration. *ACS Appl. Mater. Interfaces* **2017**, *9*, 5757–5767. [\[CrossRef\]](#) [\[PubMed\]](#)
8. Wu, C.; Chang, J. A Review of Bioactive Silicate Ceramics. *Biomed. Mater.* **2013**, *8*, 032001. [\[CrossRef\]](#)

9. Apelt, D.; Theiss, F.; El-Warrak, A.O.; Zlinszky, K.; Bettschart-Wolfisberger, R.; Bohner, M.; Matter, S.; Auer, J.A.; von Rechenberg, B. In Vivo Behavior of Three Different Injectable Hydraulic Calcium Phosphate Cements. *Biomaterials* **2004**, *25*, 1439–1451. [[CrossRef](#)]
10. Venkatraman, S.K.; Swamiappan, S. Review on Calcium- and Magnesium-Based Silicates for Bone Tissue Engineering Applications. *J. Biomed. Mater. Res. Part A* **2020**, *108*, 1546–1562. [[CrossRef](#)]
11. Devi, K.B.; Tripathy, B.; Kumta, P.N.; Nandi, S.K.; Roy, M. In Vivo Biocompatibility of Zinc-Doped Magnesium Silicate Bio-Ceramics. *ACS Biomater. Sci. Eng.* **2018**, *4*, 2126–2133. [[CrossRef](#)] [[PubMed](#)]
12. Wu, C.; Chen, Z.; Wu, Q.; Yi, D.; Friis, T.; Zheng, X.; Chang, J.; Jiang, X.; Xiao, Y. Clinoenstatite Coatings Have High Bonding Strength, Bioactive Ion Release, and Osteoimmunomodulatory Effects That Enhance in Vivo Osseointegration. *Biomaterials* **2015**, *71*, 35–47. [[CrossRef](#)] [[PubMed](#)]
13. Bakhsheshi-Rad, H.R.; Najafinezhad, A.; Hadisi, Z.; Iqbal, N.; Daroonparvar, M.; Sharif, S.; Ismail, A.F.; Akbari, M.; RamaKrishna, S.; Berto, F. Characterization and Biological Properties of Nanostructured Clinoenstatite Scaffolds for Bone Tissue Engineering Applications. *Mater. Chem. Phys.* **2021**, *259*, 123969. [[CrossRef](#)]
14. Choudhary, R.; Chatterjee, A.; Venkatraman, S.K.; Koppala, S.; Abraham, J.; Swamiappan, S. Antibacterial Forsterite (Mg₂SiO₄) Scaffold: A Promising Bioceramic for Load Bearing Applications. *Bioact. Mater.* **2018**, *3*, 218–224. [[CrossRef](#)] [[PubMed](#)]
15. Ghomi, H.; Jaberzadeh, M.; Fathi, M.H. Novel Fabrication of Forsterite Scaffold with Improved Mechanical Properties. *J. Alloys Compd.* **2011**, *509*, L63–L68. [[CrossRef](#)]
16. Jin, X.; Chang, J.; Zhai, W.; Lin, K. Preparation and Characterization of Clinoenstatite Bioceramics. *J. Am. Ceram. Soc.* **2011**, *94*, 66–70. [[CrossRef](#)]
17. Kharaziha, M.; Fathi, M.H. Synthesis and Characterization of Bioactive Forsterite Nanopowder. *Ceram. Int.* **2009**, *35*, 2449–2454. [[CrossRef](#)]
18. Zhao, F.; Zhang, L.; Ren, Z.; Gao, J.; Chen, X.; Liu, X.; Ge, T. A Novel and Green Preparation of Porous Forsterite Ceramics with Excellent Thermal Isolation Properties. *Ceram. Int.* **2019**, *45*, 2953–2961. [[CrossRef](#)]
19. Chen, L.; Ye, G.; Wang, Q.; Blanpain, B.; Malfliet, A.; Guo, M. Low Temperature Synthesis of Forsterite from Hydromagnesite and Fumed Silica Mixture. *Ceram. Int.* **2015**, *41*, 2234–2239. [[CrossRef](#)]
20. Vlasopoulos, N. Process for Producing Cement Binder Compositions Containing Magnesium. International Patent WO 2012/028471 A1, 8 March 2012.
21. Jin, F.; Al-Tabbaa, A. Strength and Hydration Products of Reactive MgO–Silica Pastes. *Cem. Concr. Compos.* **2014**, *52*, 27–33. [[CrossRef](#)]
22. Tonelli, M.; Martini, F.; Calucci, L.; Fratini, E.; Geppi, M.; Ridi, F.; Borsacchi, S.; Baglioni, P. Structural Characterization of Magnesium Silicate Hydrate: Towards the Design of Eco-Sustainable Cements. *Dalton Trans.* **2016**, *45*, 3294–3304. [[CrossRef](#)] [[PubMed](#)]
23. Martini, F.; Tonelli, M.; Geppi, M.; Ridi, F.; Borsacchi, S.; Calucci, L. Hydration of MgO/SiO₂ and Portland Cement Mixtures: A Structural Investigation of the Hydrated Phases by Means of X-Ray Diffraction and Solid State NMR Spectroscopy. *Cem. Concr. Res.* **2017**, *102*, 60–67. [[CrossRef](#)]
24. Martini, F.; Borsacchi, S.; Geppi, M.; Tonelli, M.; Ridi, F.; Calucci, L. Monitoring the Hydration of MgO-Based Cement and Its Mixtures with Portland Cement by ¹H NMR Relaxometry. *Microporous Mesoporous Mater.* **2018**, *269*, 26–30. [[CrossRef](#)]
25. Panda, B.; Sonat, C.; Yang, E.-H.; Tan, M.J.; Unluer, C. Use of Magnesium-Silicate-Hydrate (M-S-H) Cement Mixes in 3D Printing Applications. *Cem. Concr. Compos.* **2021**, *117*, 103901. [[CrossRef](#)]
26. Khalil, A.; Wang, X.; Celik, K. 3D Printable Magnesium Oxide Concrete: Towards Sustainable Modern Architecture. *Addit. Manuf.* **2020**, *33*, 101145. [[CrossRef](#)]
27. Bonini, M. Physico-Chemical Challenges in 3D Printing of Polymeric Nanocomposites and Hydrogels for Biomedical Applications. *J. Nanosci. Nanotechnol.* **2021**, *21*, 2778–2792. [[CrossRef](#)] [[PubMed](#)]
28. Weng, Y.; Ruan, S.; Li, M.; Mo, L.; Unluer, C.; Tan, M.J.; Qian, S. Feasibility Study on Sustainable Magnesium Potassium Phosphate Cement Paste for 3D Printing. *Constr. Build. Mater.* **2019**, *221*, 595–603. [[CrossRef](#)]
29. Zhao, Z.; Chen, M.; Xu, J.; Li, L.; Huang, Y.; Yang, L.; Zhao, P.; Lu, L. Mix Design and Rheological Properties of Magnesium Potassium Phosphate Cement Composites Based on the 3D Printing Extrusion System. *Constr. Build. Mater.* **2021**, *284*, 122797. [[CrossRef](#)]
30. Götz, L.-M.; Holeczek, K.; Groll, J.; Jüngst, T.; Gbureck, U. Extrusion-Based 3D Printing of Calcium Magnesium Phosphate Cement Pastes for Degradable Bone Implants. *Materials* **2021**, *14*, 5197. [[CrossRef](#)]
31. Zhao, Z.; Chen, M.; Jin, Y.; Lu, L.; Li, L. Rheology Control towards 3D Printed Magnesium Potassium Phosphate Cement Composites. *Compos. Part B Eng.* **2022**, *239*, 109963. [[CrossRef](#)]
32. Ding, Z.; Wang, X.; Sanjayan, J.; Zou, P.X.W.; Ding, Z.-K. A Feasibility Study on HPMC-Improved Sulphoaluminate Cement for 3D Printing. *Materials* **2018**, *11*, 2415. [[CrossRef](#)]
33. Buswell, R.A.; Leal de Silva, W.R.; Jones, S.Z.; Dirrenberger, J. 3D Printing Using Concrete Extrusion: A Roadmap for Research. *Cem. Concr. Res.* **2018**, *112*, 37–49. [[CrossRef](#)]
34. Hambach, M.; Rutzen, M.; Volkmer, D. Chapter 5—Properties of 3D-Printed Fiber-Reinforced Portland Cement Paste. In *3D Concrete Printing Technology*; Sanjayan, J.G., Nazari, A., Nematollahi, B., Eds.; Butterworth-Heinemann: Oxford, UK, 2019; pp. 73–113. ISBN 978-0-12-815481-6.

35. Shakor, P.; Sanjayan, J.; Nazari, A.; Nejadi, S. Modified 3D Printed Powder to Cement-Based Material and Mechanical Properties of Cement Scaffold Used in 3D Printing. *Constr. Build. Mater.* **2017**, *138*, 398–409. [\[CrossRef\]](#)
36. Sonebi, M.; Amziane, S.; Perrot, A. Mechanical Behavior of 3D Printed Cement Materials. In *3D Printing of Concrete*; John Wiley & Sons, Ltd.: Hoboken, NJ, USA, 2019; pp. 101–124. ISBN 978-1-119-61075-5.
37. Ogur, E.; Botti, R.; Bortolotti, M.; Colombo, P.; Vakifahmetoglu, C. Synthesis and Additive Manufacturing of Calcium Silicate Hydrate Scaffolds. *J. Mater. Res. Technol.* **2021**, *11*, 1142–1151. [\[CrossRef\]](#)
38. Pei, P.; Wei, D.; Zhu, M.; Du, X.; Zhu, Y. The Effect of Calcium Sulfate Incorporation on Physiochemical and Biological Properties of 3D-Printed Mesoporous Calcium Silicate Cement Scaffolds. *Microporous Mesoporous Mater.* **2017**, *241*, 11–20. [\[CrossRef\]](#)
39. Van Der Putten, J.; Deprez, M.; Cnudde, V.; De Schutter, G.; Van Tittelboom, K. Microstructural Characterization of 3D Printed Cementitious Materials. *Materials* **2019**, *12*, 2993. [\[CrossRef\]](#) [\[PubMed\]](#)
40. Gauss, C.; Pickering, K.L.; Muthe, L.P. The Use of Cellulose in Bio-Derived Formulations for 3D/4D Printing: A Review. *Compos. Part C Open Access* **2021**, *4*, 100113. [\[CrossRef\]](#)
41. Dai, L.; Cheng, T.; Duan, C.; Zhao, W.; Zhang, W.; Zou, X.; Aspler, J.; Ni, Y. 3D Printing Using Plant-Derived Cellulose and Its Derivatives: A Review. *Carbohydr. Polym.* **2019**, *203*, 71–86. [\[CrossRef\]](#) [\[PubMed\]](#)
42. Shi, S.; Jiang, Y.; Ren, H.; Deng, S.; Sun, J.; Cheng, F.; Jing, J.; Chen, Y. 3D-Printed Carbon-Based Conformal Electromagnetic Interference Shielding Module for Integrated Electronics. *Nano-Micro Lett.* **2024**, *16*, 85. [\[CrossRef\]](#)
43. Ridi, F.; Fratini, E.; Alfani, R.; Baglioni, P. Influence of Acrylic Superplasticizer and Cellulose-Ether on the Kinetics of Tricalcium Silicate Hydration Reaction. *J. Colloid Interface Sci.* **2013**, *395*, 68–74. [\[CrossRef\]](#)
44. Long, W.-J.; Tao, J.-L.; Lin, C.; Gu, Y.; Mei, L.; Duan, H.-B.; Xing, F. Rheology and Buildability of Sustainable Cement-Based Composites Containing Micro-Crystalline Cellulose for 3D-Printing. *J. Clean. Prod.* **2019**, *239*, 118054. [\[CrossRef\]](#)
45. Zaid, O.; El Ouni, M.H. Advancements in 3D Printing of Cementitious Materials: A Review of Mineral Additives, Properties, and Systematic Developments. *Constr. Build. Mater.* **2024**, *427*, 136254. [\[CrossRef\]](#)
46. Muhammad Salman, N.; Ma, G.; Ijaz, N.; Wang, L. Importance and Potential of Cellulosic Materials and Derivatives in Extrusion-Based 3D Concrete Printing (3DCP): Prospects and Challenges. *Constr. Build. Mater.* **2021**, *291*, 123281. [\[CrossRef\]](#)
47. Liu, C.; Wang, X.; Chen, Y.; Zhang, C.; Ma, L.; Deng, Z.; Chen, C.; Zhang, Y.; Pan, J.; Banthia, N. Influence of Hydroxypropyl Methylcellulose and Silica Fume on Stability, Rheological Properties, and Printability of 3D Printing Foam Concrete. *Cem. Concr. Compos.* **2021**, *122*, 104158. [\[CrossRef\]](#)
48. Schmitt, M.; Weiss, P.; Bourges, X.; Amador del Valle, G.; Daculsi, G. Crystallization at the Polymer/Calcium-Phosphate Interface in a Sterilized Injectable Bone Substitute IBS. *Biomaterials* **2002**, *23*, 2789–2794. [\[CrossRef\]](#) [\[PubMed\]](#)
49. Plank, J.; Sakai, E.; Miao, C.W.; Yu, C.; Hong, J.X. Chemical Admixtures—Chemistry, Applications and Their Impact on Concrete Microstructure and Durability. *Cem. Concr. Res.* **2015**, *78*, 81–99. [\[CrossRef\]](#)
50. Wang, X.; Zhang, J.; Yang, Y.; Shu, X.; Ran, Q. Effect of Side Chains in Block Polycarboxylate Superplasticizers on Early-Age Properties of Cement Paste. *J. Therm. Anal. Calorim.* **2018**, *133*, 1439–1446. [\[CrossRef\]](#)
51. Benard, P.; Garrault, S.; Nonat, A.; Cau-dit-Coumes, C. Influence of Orthophosphate Ions on the Dissolution of Tricalcium Silicate. *Cem. Concr. Res.* **2008**, *38*, 1137–1141. [\[CrossRef\]](#)
52. Tonelli, M.; Martini, F.; Milanese, A.; Calucci, L.; Geppi, M.; Borsacchi, S.; Ridi, F. Effect of Phosphate Additives on the Hydration Process of Magnesium Silicate Cements. *J. Therm. Anal. Calorim.* **2019**, *138*, 3311–3321. [\[CrossRef\]](#)
53. ASTM C266-21; Standard Test Method for Time of Setting of Hydraulic-Cement Paste by Gillmore Needles. American Society for Testing and Materials: West Conshohocken, PA, USA, 2021.
54. Fu, Z.; Angeline, V.; Sun, W. Evaluation of Printing Parameters on 3D Extrusion Printing of Pluronic Hydrogels and Machine Learning Guided Parameter Recommendation. *Int. J. Bioprint.* **2021**, *7*, 434. [\[CrossRef\]](#)
55. Sonat, C.; Dung, N.T.; Unluer, C. Performance and Microstructural Development of MgO–SiO₂ Binders under Different Curing Conditions. *Constr. Build. Mater.* **2017**, *154*, 945–955. [\[CrossRef\]](#)
56. Brunauer, S.; Emmett, P.H.; Teller, E. Adsorption of Gases in Multimolecular Layers. *J. Am. Chem. Soc.* **1938**, *60*, 309–319. [\[CrossRef\]](#)
57. Barrett, E.P.; Joyner, L.G.; Halenda, P.P. The Determination of Pore Volume and Area Distributions in Porous Substances. I. Computations from Nitrogen Isotherms. *J. Am. Chem. Soc.* **1951**, *73*, 373–380. [\[CrossRef\]](#)
58. Walling, S.A.; Kinoshita, H.; Bernal, S.A.; Collier, N.C.; Provis, J.L. Structure and Properties of Binder Gels Formed in the System Mg(OH)₂–SiO₂–H₂O for Immobilisation of Magnox Sludge. *Dalton Trans.* **2015**, *44*, 8126–8137. [\[CrossRef\]](#)
59. Tay, Y.W.D.; Qian, Y.; Tan, M.J. Printability Region for 3D Concrete Printing Using Slump and Slump Flow Test. *Compos. Part B Eng.* **2019**, *174*, 106968. [\[CrossRef\]](#)
60. Papachristoforou, M.; Mitsopoulos, V.; Stefanidou, M. Evaluation of Workability Parameters in 3D Printing Concrete. *Procedia Struct. Integr.* **2018**, *10*, 155–162. [\[CrossRef\]](#)
61. Gillispie, G.; Prim, P.; Copus, J.; Fisher, J.; Mikos, A.G.; Yoo, J.J.; Atala, A.; Lee, S.J. Assessment Methodologies for Extrusion-Based Bioink Printability. *Biofabrication* **2020**, *12*, 022003. [\[CrossRef\]](#) [\[PubMed\]](#)
62. Fu, Z.; Naghieh, S.; Xu, C.; Wang, C.; Sun, W.; Chen, X. Printability in Extrusion Bioprinting. *Biofabrication* **2021**, *13*, 033001. [\[CrossRef\]](#)
63. Ni, S.; Chou, L.; Chang, J. Preparation and Characterization of Forsterite (Mg₂SiO₄) Bioceramics. *Ceram. Int.* **2007**, *33*, 83–88. [\[CrossRef\]](#)

64. Kumar, S.A. *Eco-Friendly Nano-Hybrid Materials for Advanced Engineering Applications*; CRC Press: Boca Raton, FL, USA, 2017; ISBN 978-1-77188-295-8.
65. Lakshmi, R. Wollastonite/Forsterite Composite Scaffolds Offer Better Surface for Hydroxyapatite Formation. *Bull. Mater. Sci.* **2019**, *42*, 1–7. [[CrossRef](#)]
66. Jin, S.; Zhou, J.; Zhao, X.; Sun, L. Quantitative Relationship between Pore Size Distribution and Compressive Strength of Cementitious Materials. *Constr. Build. Mater.* **2021**, *273*, 121727. [[CrossRef](#)]
67. Gerhardt, L.-C.; Boccaccini, A.R. Bioactive Glass and Glass-Ceramic Scaffolds for Bone Tissue Engineering. *Materials* **2010**, *3*, 3867–3910. [[CrossRef](#)] [[PubMed](#)]

Disclaimer/Publisher’s Note: The statements, opinions and data contained in all publications are solely those of the individual author(s) and contributor(s) and not of MDPI and/or the editor(s). MDPI and/or the editor(s) disclaim responsibility for any injury to people or property resulting from any ideas, methods, instructions or products referred to in the content.